Local reaction rates and surface diffusion on nanolithographically prepared model catalysts: Experiments and simulations

M. Laurin, V. Johánek, A. W. Grant, B. Kasemo, J. Libuda, and H.-J. Freund

Citation: The Journal of Chemical Physics **122**, 084713 (2005); doi: 10.1063/1.1854622
View online: http://dx.doi.org/10.1063/1.1854622
View Table of Contents: http://scitation.aip.org/content/aip/journal/jcp/122/8?ver=pdfcov
Published by the AIP Publishing

Local reaction rates and surface diffusion on nanolithographically prepared model catalysts: Experiments and simulations

M. Laurin and V. Johánek
Fritz-Haber-Institut der Max-Planck-Gesellschaft, Faradayweg 4-6, D-14195 Berlin, Germany

A. W. Grant and B. Kasemo
Department of Applied Physics, Chalmers University of Technology, S-412 96 Göteborg, Sweden

J. Libuda[a] and H.-J. Freund
Fritz-Haber-Institut der Max-Planck-Gesellschaft, Faradayweg 4-6, D-14195 Berlin, Germany

(Received 2 September 2004; accepted 9 December 2004; published online 18 February 2005)

Combining molecular beam methods and angular resolved mass spectrometry, we have studied the angular distribution of desorbing products during CO oxidation on a planar Pd/silica supported model catalyst. The model catalyst was prepared by means of electron beam lithography, allowing individual control of particle size, position, and aspect ratio, and was characterized by atomic force microscopy and scanning electron microscopy before and after reaction. In the experiment, both oxygen and CO rich regimes were investigated using separate molecular beams for the two reactants. This allows exploration of diffusion effects of reactants on the particles and of shadowing and backscattering phenomena. A reaction-diffusion model was developed in order to extract information about local reaction rates on the surface of the catalyst nanoparticles. The model takes into account the structural parameters of the catalyst as well as the backscattering of the reactants and products from the support. It allows a quantitative description of the experimental data and provides a detailed understanding of temperature and reactant flux dependent effects. Moreover, information on the surface mobility of oxygen under steady-state reaction conditions could be obtained by comparison with the experimental results. © *2005 American Institute of Physics*. [DOI: 10.1063/1.1854622]

I. INTRODUCTION

Many heterogeneous catalysts are based on nanometer-sized metal particles, finely dispersed on oxide supports.[1,2] Reaction kinetics on such supported particle systems can differ strongly from the kinetics on single crystal surfaces. There are many effects which can contribute to these modified kinetics, including, e.g., geometric and electronic properties or interactions with the support, which lead to changes in the adsorption and reaction properties of a catalyst particle. In addition, there are pure nanoscale effects related to kinetics, which simply arise from the limited size of the particles, i.e., even without a change of their electronic and adsorption properties. Examples for such phenomena are so-called communication effects resulting from the coupling of surface areas with different adsorption or reaction behavior via surface diffusion[3–5] or coverage fluctuations in confined surface regions.[6–9] Both are intimately related to the surface mobility of the reactants.

There are very little experimental data available on such phenomena. This lack of knowledge is a result of experimental challenges associated with studies of such kinetic effects on real catalysts. First, the enormous complexity of the surfaces of real heterogeneous catalysts often precludes detailed insights into the kinetics at the molecular and single particle level (see, e.g., Refs. 10–12). For example, a distribution of particle sizes or shapes may result in some average output, disguising phenomena occurring on individual particles. Second, only few experimental techniques can provide sufficiently detailed experimental data on the surface kinetics and on surface transport phenomena under reaction conditions. In order to overcome these problems, our group and others have recently started to apply molecular beam techniques to model catalysts (see Refs. 13–18 and references therein) that aim at revealing microscopic and molecular level effects. The model catalysts reduce the complexity of the surfaces to a controllable level. Simultaneously, the application of molecular beam methods allows the extraction of detailed kinetic data under most well defined conditions.

In this work we employ a supported model catalyst, which was prepared by electron beam lithography[19–23] (EBL). This preparation method has been used only recently in ultrahigh vacuum (UHV) reactivity studies.[6,24] It provides the advantage of the highest level of control over structural parameters, including homogeneous particle sizes, exactly controllable particle distances and positions, and variable aspect ratios.

Returning to the communication effects discussed above, these phenomena arise from the coupling of regions with locally different adsorption or reaction properties via surface diffusion (for example, facets with different crystallographic orientation on a single particle). This potentially gives rise to locally different reaction rates. The direct experimental veri-

[a]Author to whom correspondence should be addressed. Fax: +49-30-84134139. Electronic mail: libuda@fhi-berlin.mpg.de

fication of such phenomena, however, would require measurements of local reaction rates on individual parts of a catalyst particle, e.g., on the different microfacets. The development of methods, which allow local kinetic experiments, is a major challenge. As a possible alternative approach, we have recently suggested the application of angular resolved measurements of the desorbing products from a planar model catalyst with arrays of identical or nearly identical particles.[24,25] The basic idea is that the angular distribution may contain information on the local reaction rates on differently oriented facets of the particles.

We have chosen the CO oxidation on Pd particles as model reaction. The mechanism and kinetics of CO oxidation on platinum metals are well understood.[26,27] In general, oxygen adsorbs dissociatively and CO molecularly, with CO having a strongly inhibiting effect on the oxygen adsorption. From the two adsorbed species, CO_2 is formed in a Langmuir–Hinshelwood (LH) reaction step. The surface mobilities of both reactants are rather different. The diffusion barriers are low for adsorbed CO on platinum metal surfaces, leading to high mobility, even at low sample temperature.[28,29] The diffusion activation energies for the adsorbed oxygen are significantly higher (see, e.g., Ref. 28). As a result, CO diffusion is expected to be fast as compared to reaction. For oxygen, on the other hand, surface diffusion and surface reaction may occur on the same time scale, or reaction may even be fast as compared to diffusion.

A critical point for the present experiment is that the CO_2 product interacts only weakly with the metal surface, leading to nearly instant desorption after formation. Moreover, desorption is typically found to be preferentially directed along the surface normal for close-packed surfaces (the exact distribution may depend on the local surface and adsorbate structure).[26,30] Consequently, the angular distribution of CO_2 can be assumed to directly reflect the distribution of local reaction rates on the particles.

In a recent work, we have demonstrated qualitatively that this method can indeed provide the desired information.[24] It was shown that pronounced dependences of the angular distribution of the desorbing CO_2 can be observed for sufficiently large Pd particles. Previous analysis of the angular distributions, however, was limited to a simple and qualitative model. In this work, we present details on the preparation method and on the experimental approach. We further develop a microkinetic model, which is capable of a quantitative description of the experimental results.

II. EXPERIMENT

A. Electron beam lithography

The fabrication of nanoparticles by EBL has recently been used successfully in surface science and catalysis (e.g., Refs. 19–23). The advantage of the method is that it provides ultimate control over structural parameters such as particle size, shape, and separation, as compared to more traditional preparation methods, such as physical vapor deposition. It is a serial technique in which an electron beam is rastered across the surface of an electron sensitive polymeric film (resist), creating a computer generated pattern in this film. A

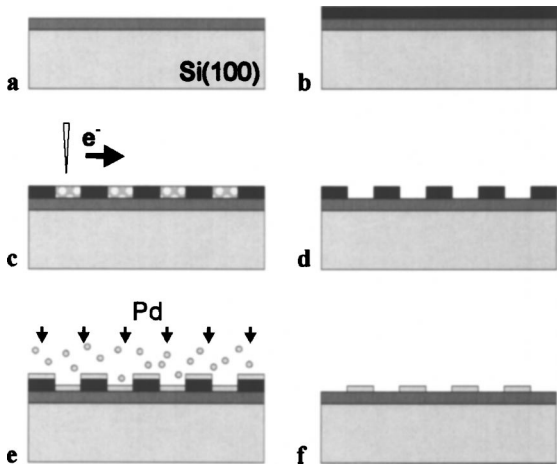

FIG. 1. Electron beam lithographic (EBL) preparation of a model catalyst: (a) cleaning of the Si(100) substrate with a 0.4 μm thick oxide layer; (b) spin coating of a photoresist layer; (c) exposure to a predesigned pattern with an electron beam; (d) development, i.e., dissolution of the photoresist; (e) Pd evaporation; (f) lift-off, i.e., dissolution of the remaining resist.

schematic diagram of the EBL procedure is shown in Fig. 1. In this work, we used a 0.4 μm thick thermal oxide layer grown on Si(100) as the substrate. The Pd towers were fabricated with a double layer resist system, consisting of a bottom layer of PMGI-SF7 (polyimide) and top layer of 1:2 diluted ZEP520 in anisole. The pattern was exposed with a dose of 160 μC cm^{-2} in an EBL system (JEOL JBX9300FS). After dissolving the exposed polymer, a 500 nm thick film of Pd (99.95% purity, K.A. Rasmussen, AB) was vapor deposited at $\sim 3\times10^{-6}$ mbar at a flux of $\sim$8 Å s^{-1} as measured by a quartz crystal microbalance in an electron beam deposition system (AVAC HVC-600). The remaining resist was "lifted-off" in Shipley 1165 (*N*-methyl-2-pyrrolidone) leaving the Pd towers in the prescribed pattern (Fig. 1). After resist removal, the sample was cleaned for 1 h at 770 K in 5% O_2 in Ar, followed by 1 h at 820 K in 2% H_2 in Ar at a flow rate of $\sim$500 ml min^{-1} in a flow reactor, and cooled in Ar, which removed $\sim$70% of the contaminants according to XPS.

The EBL sample was fabricated at the Chalmers University of Technology and transported to the FHI, where the molecular beam experiments were performed. The sample was further cleaned in the molecular beam UHV apparatus (described in Sec. II B) by exposure to $\sim 4\times10^{-4}$ mbar O_2 from a gas doser for 2 h at a sample temperature of 650 K and subsequent oxygen removal by CO exposure. Finally, the cleanliness of the Pd particles was checked by means of CO titration. For this purpose, the sample was exposed to a molecular beam of O_2 ($\sim 3\times10^{14}$ molecules cm^{-2} s^{-1}, 30 s) at room temperature, followed by titration at 440 K with a molecular beam of CO ($\sim 2.9\times10^{14}$ molecules cm^{-2} s^{-1}, 30 s). The amount of CO_2 produced was compared to the value expected on the basis of the Pd surface area calculated from the structural parameters of the sample and the O saturation coverage.[31,32]

The sample fabricated by EBL consists of $\sim$450 nm high Pd towers with $\sim$500 nm diameter. The particles are arranged in a hexagonal array with 1500 nm particle separation (center to center) covering 1 cm^2 area (Fig. 2). The mor-

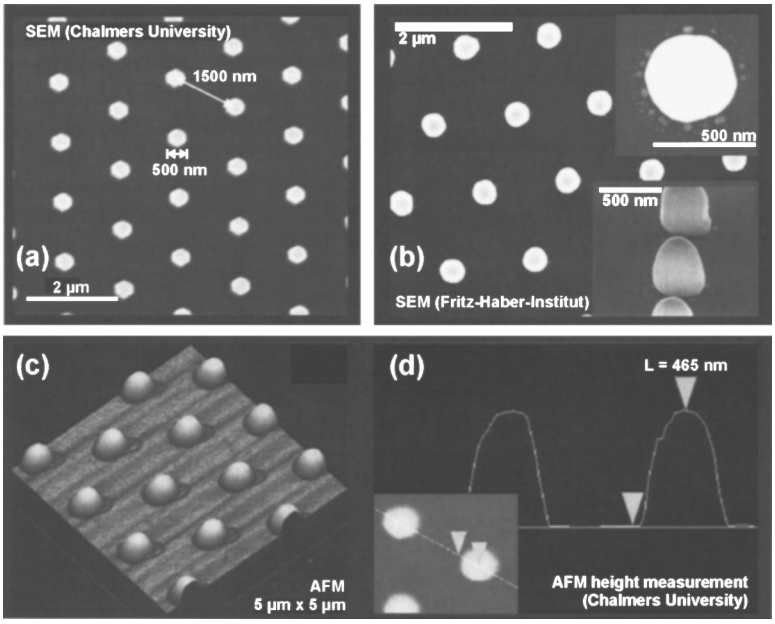

FIG. 2. SEM images of the Pd/silica model catalyst prepared by EBL (a) before and (b) after reaction, note the faceting and the ring of small Pd particles surrounding every big particle (see text for discussion); (c) AFM image and (d) AFM height measurement of the particles.

phology of the particles was investigated by SEM (scanning electron microscopy) and AFM (atomic force microscopy) prior and by SEM after the experiments to verify that no major morphological changes occurred (as has been observed, e.g., in Ref. 19 under more drastic reaction conditions).

A close inspection reveals a ring of small Pd islands surrounding every Pd tower. This effect is likely due to reshaping of the polycrystalline particles toward the Wulff shape in the annealing and cleaning sequences during which the small aggregates may split off the central particle.[19,20,33] Similar effects have been observed previously for Pt model catalysts prepared by EBL. From SEM images [Fig. 2(b)], the surface ratio of primary EBL particles to the split-off particles can be estimated as ~5. As a result, the CO oxidation should under all conditions be dominated by the primary particles. In particular as the CO oxidation shows a weak structure dependence, so that no enhanced activity of smaller particles is expected. Furthermore, small split-off particles may only give rise to an additional symmetric contribution to the CO_2 signal, which should not critically affect the angular resolved results discussed in the following.

B. Molecular beam apparatus

The experiments were performed in the UHV molecular beam apparatus at the FHI already described in Ref. 34. Briefly, the molecular beam of CO was generated by an effusive beam source (EB) (incidence angle $\phi=0°$, $\gamma=35°$, see Fig. 3 for details of the experimental setup). Isotopically marked ^{13}CO (min 99% ^{13}CO, Isotec Inc.) was used in order to reduce the background level. It was further purified by a Waferpure MiniXL WPMV200CO, Mykrolis GmbH filter. The O_2 (99.9995%, Linde AG) beam was provided by a supersonic source (SSB) at large incidence angle ($\phi=60°$ from the surface normal, $\gamma=0°$, Fig. 3). This experimental setup ensures that one side of the particles is completely shaded from a direct O_2 flux. The $^{13}CO_2$ (we drop the superscript in the following) signal was recorded simultaneously by a line-of-sight angular resolved quadrupole mass spectrometer (QMS) (doubly differentially pumped), and in an angular integrated fashion by a non-line-of-sight QMS (Fig. 3). The angle ϕ is measured between the surface normal and the angular resolved QMS with positive ϕ directed toward the O_2 beam and negative ϕ toward the shaded side. Angles +35° to +90° are not accessible experimentally because in this range the SSB is shadowed by the angular resolved QMS.

III. MOLECULAR BEAM EXPERIMENTS

A. Experimental procedure

In order to extract the angular distribution of the desorbing CO_2, we apply a method which has already been briefly

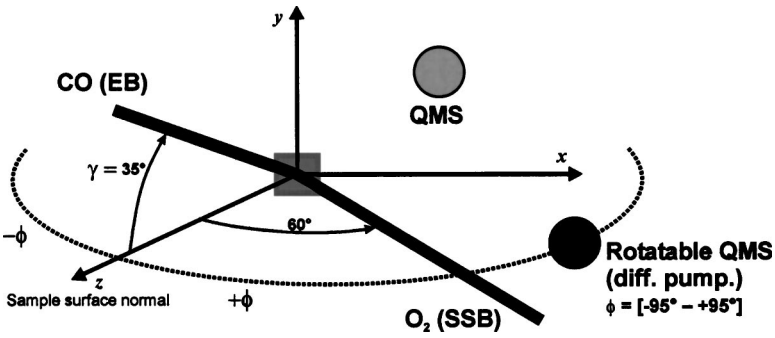

FIG. 3. Molecular beam apparatus used for the experiments: two molecular beams [one generated by an EB and one generated by a supersonic source (SSB)] are superimposed on the sample surface, the reaction rate is measured by means of a line-of-sight rotatable mass spectrometer (QMS) and a non-line-of-sight mass spectrometer (QMS).

described in the literature[34] (see Fig. 4). After steady state is established for a given set of reaction conditions, the CO_2 signal is measured on the front side of the sample from $\phi = -90°$ to $\phi = +90°$ by the angular resolved QMS [Fig. 4(a)]. The diffuse background of CO_2 is determined on the backside of the sample at $\phi = -95°$ and $\phi = +95°$ and linearly subtracted from the signal. For comparison, the data are then normalized with respect to few points around $\phi = 0°$ [Figs. 4(a) and 4(b)].

The acceptance area of the angular resolved detector changes as a function of the detection angle.[35] We determine the detector function by using a well defined angular distribution, i.e., the one of Ar scattered from a flat sample covered by a thick ice (H_2O) layer at a surface temperature of $T = 100$ K. As Ar trapping is complete under these conditions,[36] detailed balance requires that the angular resolved distribution of the desorbing Ar is cosine [Fig. 4(c)]. Consequently, the CO_2 signal is normalized to the ratio of the Ar signal and a cosine distribution. The angular distribution of the desorbing CO_2 flux obtained in this fashion is plotted in Fig. 4(d).

B. Experimental results and discussion

A summary of the experimental results obtained via the procedure described in Sec. III A is provided in Fig. 5. Here, we focus on the most essential observations. For more detailed results and discussions we refer to the previous publications.[24,25]

The global reaction kinetics is illustrated in Fig. 5(a). The steady-state reaction rates were measured in an angular integrated fashion by the non-line-of-sight QMS as a function of the fraction of CO in the incident flux $x_{CO} = F_{CO}/(F_{CO} + F_{O2})$. Here, F_{CO} and F_{O2} are the fluxes of CO and O_2 at the sample position. The total flux in this experiment was kept constant and is equivalent to a pressure of $\sim 10^{-4}$ Pa.

Up to $x_{CO} \approx 0.5$, the CO_2 production rate increases linearly with x_{CO}. This regime, denoted in the following as the O-*rich* regime, is characterized by a low Θ_{CO} (CO coverage; Θ_O denotes the oxygen coverage) on particle surface.[37] At higher x_{CO}, the kinetics switches to the so-called CO-rich regime characterized by a higher Θ_{CO} and a lower Θ_O. At lower surface temperatures, the transition to the CO-rich regime is connected to a substantial decrease in the reaction rate. This effect is due to inhibition of oxygen adsorption by preadsorbed CO. At higher temperatures, the CO desorption rate increases and the CO inhibition vanishes [Fig. 5(a)].

In the following, we investigate the angular distribution of the desorbing CO_2 in both regimes, O rich and CO rich. The experiments were performed at a constant O_2 flux of $F_{O2} = 5.6 \times 10^{14}$ cm^{-2} s^{-1} and CO fluxes of $F_{CO} = 2.9 \times 10^{14}$ cm^{-2} s^{-1} (O-rich regime, $x_{CO} = 0.34$) and $F_{CO} = 11.6 \times 10^{14}$ cm^{-2} s^{-1} (CO-rich regime, $x_{CO} = 0.67$). The resulting total gas fluxes are equivalent to pressures in the range 10^{-4}–10^{-3} Pa.

The angular distributions of CO_2 are displayed in Fig. 5(c). Under O-rich conditions, the distribution is symmetric.

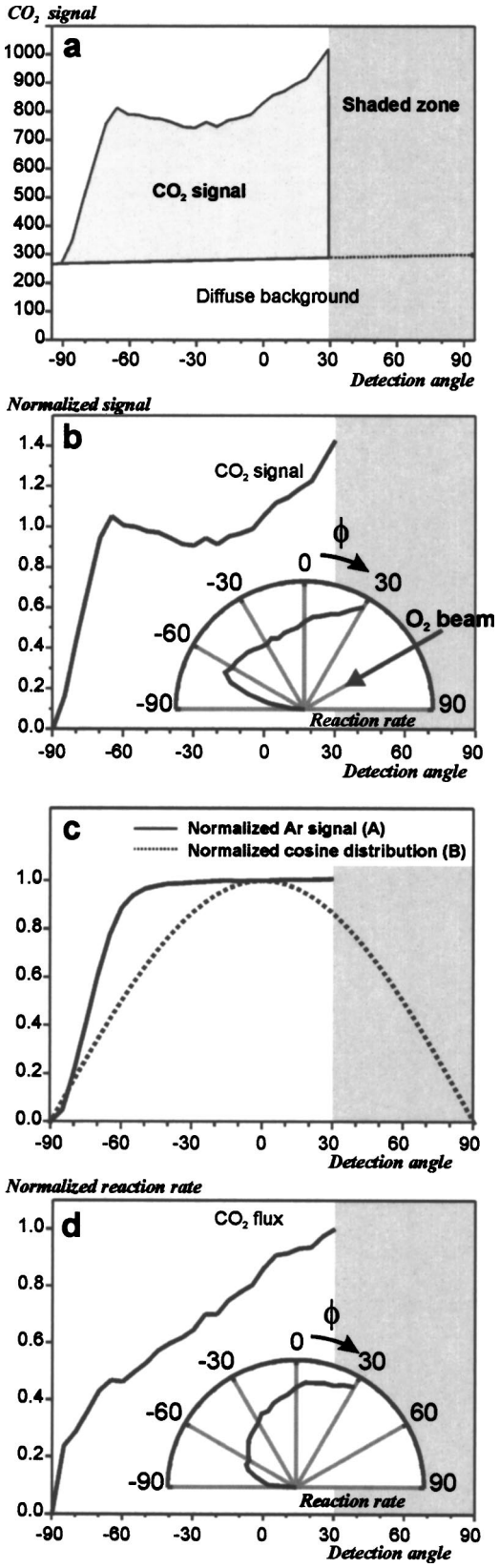

FIG. 4. Experimental data analysis: (a) Signal measured by the angular resolved QMS from −95° to +95°; (b) normalized signal after background subtraction (inset on a polar plot); (c) Ar signal backscattered from an ice covered sample at 100 K and theoretical cosine distribution (see text); (d) angular distribution of the CO_2 desorption rate after correction for the experimentally derived detector function (inset on a polar plot). In the gray zone, the O_2 beam is shaded by the angular resolved QMS.

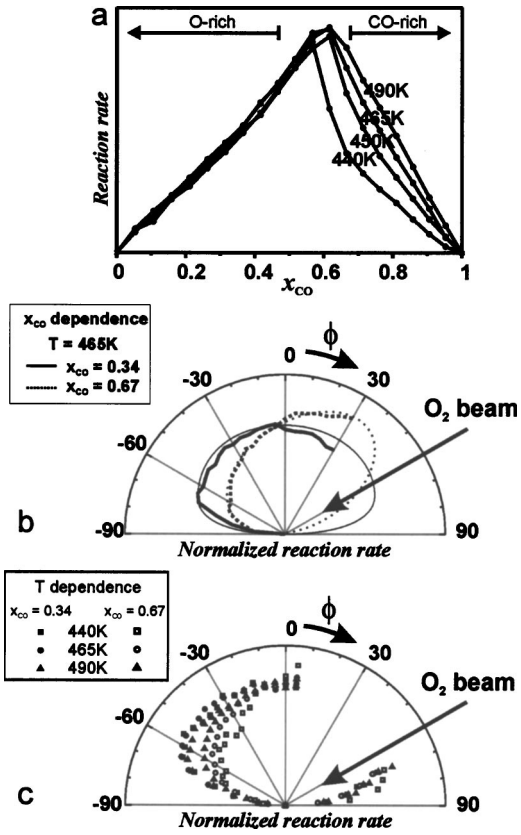

FIG. 5. Experimental data on the angular distribution of desorbing CO_2: (a) global production rate as a function of x_{CO} for temperatures $T=440$, 450, 465, and 490 K; (b) angular dependence of the CO_2 production rate as a function of x_{CO} (see text); plain line, O-rich regime; dotted line, CO-rich regime; (c) dependence on surface temperature.

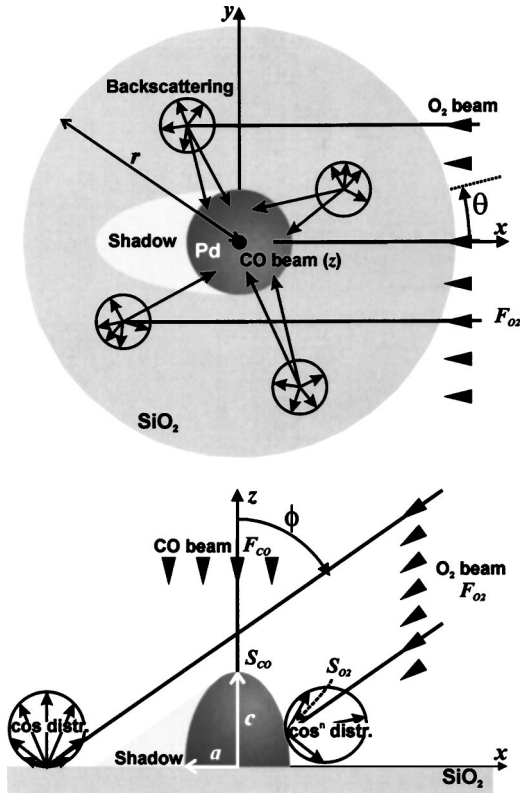

FIG. 6. Geometric model used in the microkinetic simulations: the Pd particle is represented by a half prolate spheroid (polar radius $c=450$ nm, equatorial radius $a=250$ nm) sitting on a support disk of $r\approx 25$ μm diameter. The CO flux is incident from $\phi=0°$ and the O_2 flux from $\phi=60°$, $\theta=0°$ thus creating an area around $\theta=180°$ where the particle and the support receive no direct flux from the O_2 beam. The backscattering of the reactants and products from the support is also included in the model.

In contrast, a strong asymmetry is observed under CO-rich conditions, with a higher CO_2 production rate on the particle side facing the O_2 beam.

The critical quantities, which explain these results, are the diffusion lengths of CO and oxygen on the time scale of the residence times of the adsorbates on the surface. In the O-rich regime under steady-state conditions, the large Θ_O leads to large oxygen residence times and thus to large diffusion lengths (before reaction occurs). Thus, Θ_O is equilibrated over the whole particle surface. Under CO-rich conditions, however, Θ_O is significantly smaller. This leads to drastically reduced residence times and diffusion lengths. Under these conditions there is no equilibration of Θ_O on the particle. Consequently, Θ_O and CO_2 production are enhanced on the particle side directly exposed to the O_2 beam (see Ref. 24 for details). In contrast, CO diffusion is much faster and the diffusion length is expected to exceed the particle size, both under CO- and O-rich conditions.

The surface temperature dependence of the angular distributions of CO is shown in Fig. 5(c). (Note that a slightly different experimental geometry was used, for details see Ref. 24.) Only weak temperature dependent effects are observed in the angular distribution, in contrast to the strong dependence on x_{CO}. The symmetric distribution under O-rich conditions is nearly independent of temperature. The asymmetry observed under CO-rich conditions is found to become slightly less pronounced with increasing surface temperature.

Under O-rich conditions, the missing temperature dependence points to the fact that the O diffusion length exceeds the particle size. The weak temperature dependence under CO-rich conditions is more difficult to understand and is partly the result of a compensation effect, discussed in Sec. IV D.

IV. MICROKINETIC SIMULATIONS

A. Description of the model

In order to model the experimental data, we start from a mean field approach[38] and add scattering and surface diffusion processes. The reaction-diffusion model is illustrated in Fig. 6. The catalyst particle (diameter 500 nm, height 450 nm) is represented by a half prolate spheroid (polar radius $c=450$ nm, equatorial radius $a=250$ nm). The support is described by a disk of radius ~ 25 μm. For the numerical treatment, the system is discretized using spherical coordinates in a (r,θ,ϕ) system where r is the radius, $0\leqslant\theta<2\pi$ the azimuth, and $0\leqslant\phi\leqslant\pi$ the colatitude (Fig. 6). The particle is divided into 400 surface elements ($\theta\times\phi=20\times 20$) and the support into 20 000 surface elements ($r\times\theta=1\,000\times 20$).

The microkinetic model used to describe the reaction is based on the experimental information available on the CO oxidation on Pt group metals (see the Introduction). The simple mean field description was previously developed to

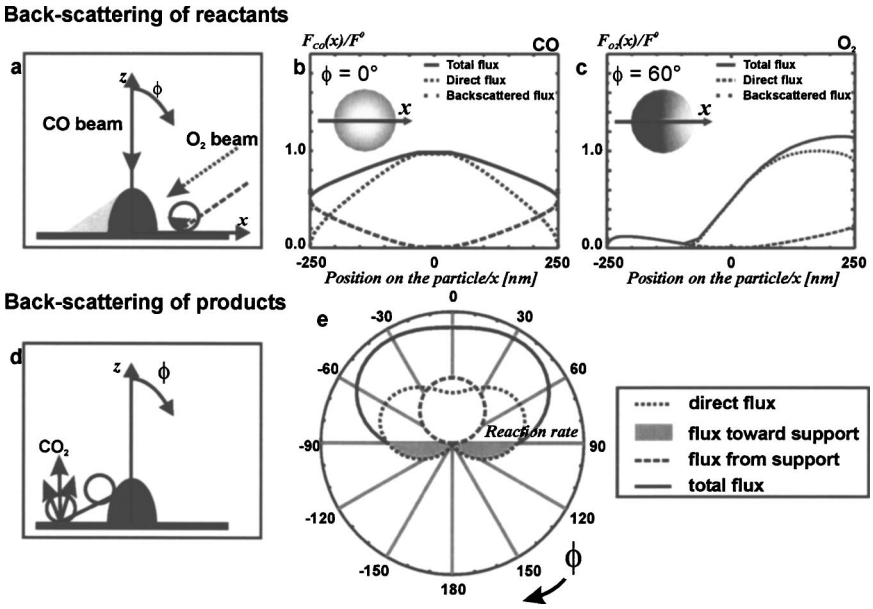

FIG. 7. (a) Model for the incoming reactant fluxes: (b) CO flux at the surface of the particle (direct and backscattered, see text) and (c) O_2 flux (direct and backscattered). (d) Model for the outgoing CO_2 flux: the CO_2 flux emitted from the particle over the unit sphere surrounding the particle (dotted line); (e) 2D cut through the particle containing the *xz* plane; values at the top side constitute the direct flux; values at the bottom side are integrated and reemitted with a cosine distribution toward $\phi=0$, constituting the backscattered flux; the direct and backscattered fluxes are summed (line) and yield the total angular CO_2 distribution.

describe the CO oxidation kinetics on a Pd catalyst as a function of reactant flux and surface temperature.[38,39] This model is capable of quantitatively reproducing both the steady-state and the transient kinetics. In future work, an extension of the microkinetic description to kinetic effects beyond the mean field approximation would be possible on the basis of Monte Carlo models.[25,40,41] In some cases, such effects have been shown to play an important role (see, e.g., Ref. 42).

For the present model catalyst, some kinetic parameters were adjusted to quantitatively reproduce the angular integrated kinetics. Briefly, the steps are as follows (see Ref. 39 for details): (i) CO adsorbs on the metal with a sticking coefficient S_{CO}, modeled by a Langmuir molecular adsorption term (a weak dependence of S_{CO} on Θ_O is taken into account); (ii) O_2 adsorbs dissociatively with a sticking coefficient S_{O2}, modeled by a Langmuir dissociative adsorption term; (iii) the LH reaction step between the adsorbed species proceeds with a reaction rate k_{LH} with an Arrhenius-type temperature dependence (activation energy E_{LH}, preexponential factor A_{LH}); (iv) CO can desorb from the metal with a rate constant k_{des} [Arrhenius-type temperature dependence, activation energy E_{des}, preexponential factor A_{des}; a factor (α_{CO}) describing the coverage dependence of E_{des} is used]; (v) O_2 desorption can be neglected in the temperature range considered; and (vi) CO_2 interacts weakly with the metal surface, resulting in desorption immediately after formation.[26] Θ_{CO} and Θ_O are defined with respect to an atom density of $N_{Pd}=1.53\times10^{15}$ cm^{-2} as in Ref. 39, corresponding to the surface atom density of Pd(111). A fitting of the model with respect to the global steady-state rates as a function of the surface temperature and x_{CO} leads to the following parameters: $E_{des}=142$ kJ mol^{-1}, $A_{des}=4\times10^{14}$ s^{-1}, $\alpha_{CO}=0.12$; $E_{LH}=53$ kJ mol^{-1}; $A_{des}=5\times10^{7}$ s^{-1}; initial sticking coefficients $S^0_{CO}=0.7$ and $S^0_{O2}=1-[7.4\times10^{-4}\times T\,(\mathrm{K})]$ (the latter includes a dependence on the surface temperature); other parameters as in Ref. 38.

In a first step, the reactant fluxes (F_{CO},F_{O2}) are calculated at each surface element of the particle and of the support. F_{CO} is incident from $\phi=0°$, leading to a symmetric flux distribution. F_{O2} is incident from $\theta=0°$, $\phi=60°$. The latter results in the shading of parts of the particle on the side opposite to the beam, i.e., some surface elements do not receive any direct flux of O_2. In addition to the direct flux, molecules can impinge on the support. As the interaction of both reactants with SiO_2 is weak, CO and O_2 might either be trapped for a short time in a physisorbed state on the support and subsequently desorb (trapping/desorption channel) or might be directly backscattered into the vacuum (direct inelastic scattering channel). We do not distinguish between these processes and we refer to the sum of both channels as the backscattering component from the support. Moreover, there is no explicit incorporation of molecules trapped on the support and diffusing to the particles (see below). A fraction of this backscattered flux collides with the Pd particles and leads to an additional CO and O_2 flux. This is particularly relevant on the parts of the catalyst particle which receive no or little direct flux. The backscattering contribution is modeled assuming a cosine distribution from the support for both CO and O_2. This assumption is justified by the fact that the SiO_2 support is rough on the atomic scale and both trapping-desorption and direct scattering channels are expected to be rather diffuse. It should be noted that the backscattered fluxes onto the particle are different for O_2 and CO, due to the shadow of the particle on the support, which has to be taken into account for O_2 (see Figs. 6 and 7). The role of support backscattering for the present type of experiments is investigated in detail in Sec. IV E. After establishing the local reactant fluxes, the nonspatial part of

$$\frac{d\Theta_{CO}}{dt}=\frac{F_{CO}}{N_{Pd}}S_{CO}-k_{des}\Theta_{CO}-k_{LH}\Theta_{CO}\Theta_O,$$

$$\frac{d\Theta_O}{dt}=2\frac{F_{O2}}{N_{Pd}}S_{O2}-k_{LH}\Theta_{CO}\Theta_O+\nabla(D\nabla\Theta_O) \quad (1)$$

can be integrated for any initial (Θ_{CO},Θ_O) distribution. In a second step, the spatial part of Eq. (1) is integrated using the

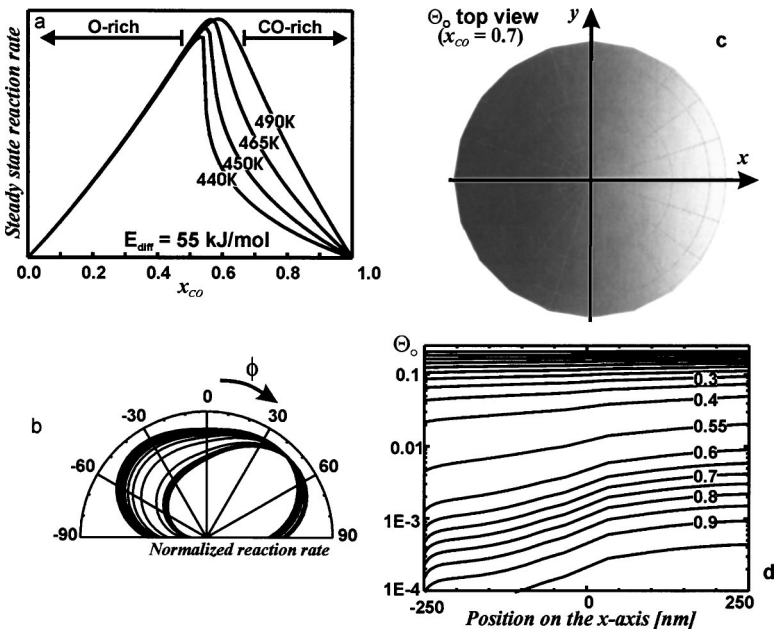

FIG. 8. Simulated data: (a) steady-state reaction rate as a function of x_{CO} ($T=440$, 450, 465, and 490 K, $E_{diff}=55$ kJ mol^{-1}); (b) angular distribution of desorbing CO_2 in the O-rich regime ($x_{CO}<0.5$), the angular distribution is symmetric, switching to an asymmetric distribution under CO-rich condition ($x_{CO}>0.6$) (x_{CO}, from 0.05 to 0.95 in steps of 0.05; see text); (c) example of oxygen coverage distribution on the surface of the particle (top view, CO-rich regime; black, low O coverage; white, high O coverage); (d) oxygen concentration profiles as a function of x_{CO}; (b–d) $T=465$ K, $E_{diff}=55$ kJ mol^{-1}.

finite element method with periodic boundary conditions on θ and no flux across $\phi=90°$, $\forall\ \theta$. The physical meaning of the latter is that we do not take surface diffusion from the oxide to the particle or vice versa into account. This simplification is justified by the large particle size and by the weak interaction of the reactants with the support. Estimates of the size of adsorbate capture zones on similar systems under reaction conditions are typically in the range of a few nanometers.[43,44] Thus, we expect that the adsorbate flux via surface diffusion over the particle/support interface is negligible as compared to the direct flux.

An Arrhenius temperature dependence of the oxygen diffusion coefficient D is assumed,

$$D = D_0 \exp\left(\frac{E_{\mathrm{diff}}}{RT}\right),$$

with E_{diff} representing the diffusion activation energy. Little experimental data are available on the diffusion coefficient for oxygen on Pd(111). We thus assume a "normal" prefactor of $D_0=10^{-7}$ m^2 s^{-1}.[28] The effect of E_{diff} on the angular distribution of CO_2 is investigated in Sec. IV C. It is found that a value of $E_{diff}=(55\pm10)$ kJ mol^{-1} is in good agreement with our experimental results. This value is also consistent with previous estimates[24,25] and with theoretical investigations.[45] This value is used for the simulations unless otherwise stated. For simplicity, we neglect coverage dependences of the diffusion coefficient D.

As pointed out before, the diffusion barrier for CO on close packed noble metal surfaces is in general small.[28] This leads to a high CO mobility, even at low surface temperature. For CO/Pd(111) a value of 175 meV was found by Snabl *et al.*[29] Θ_{CO} is therefore averaged to $\overline{\Theta_{CO}}$ over the surface of the particle. After every integration step, we obtain a couple $(\Theta_O, \overline{\Theta_{CO}})$ from which the CO_2 production for each surface element of the particle is calculated as $r_{CO2}=k_{LH}\overline{\Theta_{CO}}\Theta_O$.

The angular distribution of the desorbing CO_2 from a Pd area element is modeled by a $\cos^n\phi$ distribution. $n=1$ was found experimentally for CO oxidation on Pd(111) in the limit of low adsorbate coverages.[26] However, more highly directed distributions are possible at higher coverages.[30] In Sec. IV F we investigate the effect of the local CO_2 distribution on the type of angular resolved experiments discussed in this work. In general, $n=1$ is in good agreement with our experimental results.

In analogy to the reactants, CO_2 can be emitted into the vacuum or collide with the support upon desorption (see Figs. 6 and 7). In latter case trapping/desorption is also taken into account. The product backscattering depends on both the CO_2 distribution and the particle shape. The total CO_2 flux towards the support is calculated by integration over the lower half unit sphere. Afterwards, the flux is reemitted into the vacuum assuming a cosine distribution. The direct and the backscattered product channels are added and constitute the full CO_2 angular distribution.

B. Influence of the CO/O_2 ratio

We validate the kinetic model by simulating the global steady-state reaction rates as a function of x_{CO} and surface temperature (by integration over the full particle surface) [Fig. 8(a)]. A comparison with the experimental data is plotted in Fig. 5(a). It shows a good agreement under all conditions. Both the temperature dependence and the transition point between the two regimes are well reproduced.

Next, we investigate the local variation of Θ_O and the reaction rates. The steady-state oxygen coverage on the surface of the catalyst particle at $T=465$ K and $x_{CO}=0.7$ (CO rich conditions) is displayed in Fig. 8(c) (white: high Θ_O, black: low Θ_O). Θ_O is significantly higher on the side facing the O_2 beam. This indicates that Θ_O is not equilibrated over the surface under these conditions. Θ_O profiles along the x axis ($y=0$) are displayed in Fig. 8(b) for various x_{CO} values. Under O-rich conditions ($x_{CO}<0.4$), the Θ_O profiles are almost flat. With decreasing x_{CO} they approach saturation coverage ($\Theta_O^{max}=0.25$). With increasing x_{CO}, Θ_O decreases and a gradient in Θ_O appears. Once we approach the transition

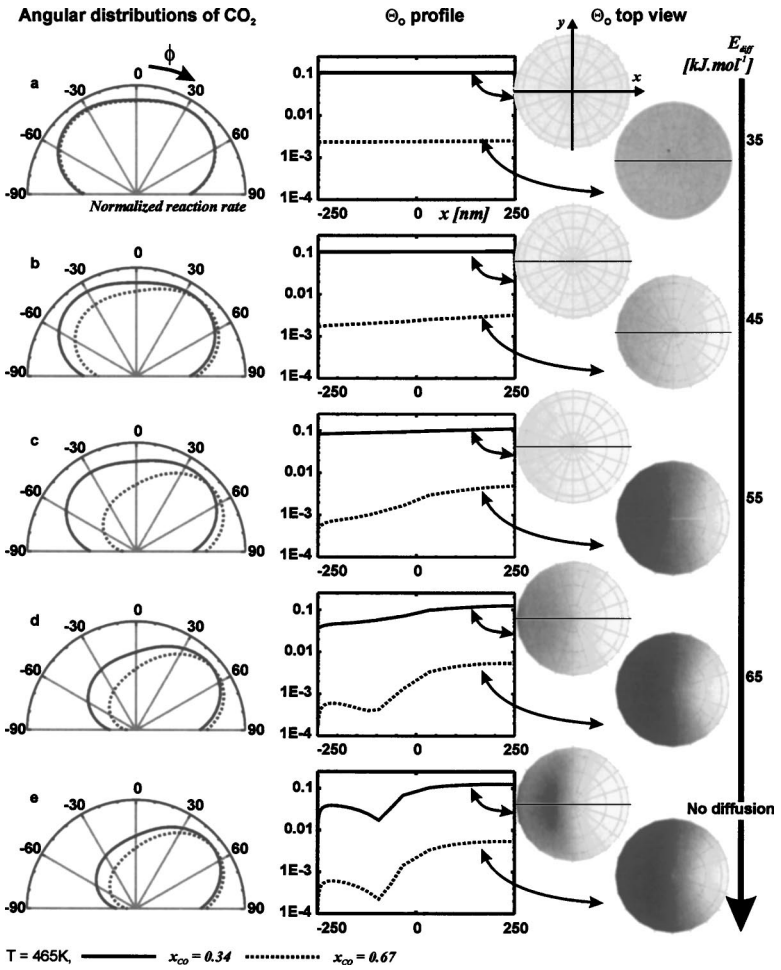

FIG. 9. The role of oxygen surface diffusion investigated at $T=465$ K; $E_{\mathrm{diff}}=35$ kJ mol^{-1} (a), 45 kJ mol^{-1} (b), 55 kJ mol^{-1} (c), 65 kJ mol^{-1} (d), and without oxygen diffusion (e); the two regimes O-rich ($x_{\mathrm{CO}}=0.34$) and CO-rich ($x_{\mathrm{CO}}=0.67$) are compared. Left to right: Angular distribution of CO_2, Θ_O along the x axis of the particle and top view of Θ_O distribution on the particle surface (white, high Θ_O; black, low Θ_O).

between the O-rich and the CO-rich regimes ($0.4<x_{\mathrm{CO}}<0.6$), the Θ_O profiles change rapidly and the Θ_O ratio between the shaded side and the beam side becomes very large. Within the CO-rich regime ($x_{\mathrm{CO}}>0.6$), the gradient in $\ln\Theta_O$ ($d\ln\Theta_O/dx$) is nearly constant while $\ln\Theta_O$ decreases rapidly [Fig. 8(c)].

As discussed in our previous work,[24] this behavior can be easily understood qualitatively: On both sides of the transition point between the CO-rich and the O-rich regimes, the reaction rates are comparable. Simultaneously, Θ_O changes by approximately two orders of magnitude between $x_{\mathrm{CO}}=0.3$ and $x_{\mathrm{CO}}=0.7$. A similar change follows for the oxygen residence time. As a result, the diffusion length of the adsorbed oxygen decreases dramatically. Consequently, no complete equilibration occurs and a switching from a symmetric to an asymmetric angular distribution is observed.

As Θ_{CO} is assumed to be constant over the particle, the differences in Θ_O directly reflect the changes in local reaction rate. In order to compare these results with the experiments, the resulting CO_2 angular distributions have to be calculated (taking into account the local angular CO_2 distribution and possible support backscattering of the products).

The corresponding simulations are displayed in Fig. 8(d). As expected, we obtain broad symmetric CO_2 distributions in the limit of small x_{CO} values (O rich). With increasing x_{CO}, nearly no changes in the angular distributions are observed until the transition to the CO-rich regime occurs. Here, the angular distributions rapidly change towards an asymmetric shape, with a strongly enhanced CO_2 production on the particle side facing the O_2 beam. After switching to the CO-rich regime, a further increase in x_{CO} only leads to minor changes in the angular distributions. In terms of the Θ_O profiles discussed above, this is a result of the constant gradient in $\ln\Theta_O$ with increasing x_{CO}. Comparison of the simulations to the experiments displayed in Fig. 5(b) shows that the angular distributions and their behavior as a function of x_{CO} is well reproduced.

C. Influence of the surface diffusion rate

In our previous work, we have given an estimate of the diffusion activation energy for oxygen E_{diff} based on residence times and diffusion lengths from a simple mean field model.[24] The present reaction-diffusion model allows us to refine this analysis by a direct comparison to the experimental angular distributions. We simulate CO_2 angular distributions for diffusion activation energies ranging from 35 kJ mol^{-1} to the case of "immobile" oxygen (see Fig. 9) under the conditions applied in the experiments (i.e., $x_{\mathrm{CO}}=0.34$; $x_{\mathrm{CO}}=0.67$; $T=465$ K). Focusing on the Θ_O profiles first, it is seen that for diffusion activation barriers of 35 kJ mol^{-1} and below, the oxygen distribution is homogeneous, both under CO- and O-rich conditions. This indicates an equilibration of Θ_O over the particle surface independent

of the reaction conditions. As a consequence, the CO_2 distributions are symmetric and independent of x_{CO}. For $E_{diff}=45$ kJ mol^{-1} a weak gradient is found in the Θ_O profile under CO-rich conditions ($x_{CO}=0.67$), leading to a slight asymmetry in the CO_2 distribution. Under O-rich conditions on the contrary, the distribution remains symmetric. As discussed in the preceding section, this is a result of the oxygen residence time being typically one to three orders of magnitude larger under O-rich conditions ($x_{CO}=0.34$), thus allowing for the equilibration of Θ_O at higher E_{diff}. At $E_{diff}=55$ kJ mol^{-1} a larger Θ_O gradient is established, giving rise to a strongly asymmetric CO_2 distribution under CO-rich conditions. Conversely, the distribution still remains symmetric under O-rich conditions. For larger E_{diff} (65 kJ mol^{-1} and above), the Θ_O profiles finally show pronounced gradients both under CO-rich and O-rich conditions, leading to asymmetric distributions in both cases. In the case of immobile oxygen (no diffusion), it is noteworthy that a dip appears in the Θ_O profiles on the shaded side of the particle. This dip is the result of a minimum in the local O_2 flux impinging on the particle. The total local flux is the sum of the direct beam flux and the backscattering of reactants from the support. As a result of the particle geometry, latter contribution is enhanced in the vicinity of the particle support boundaries. This effect is discussed in detail in Sec. IV E.

As shown in Sec. III B and Ref. 24, the experimental CO_2 distributions exhibit a fully symmetric distribution for $x_{CO}=0.34$ (O-rich) and a pronounced asymmetry for $x_{CO}=0.67$ (CO-rich). A comparison between the experiments and the simulations allows us to obtain an estimate of the activation energy for the oxygen diffusion under reaction conditions of (55 ± 10) kJ mol^{-1}. The lack of experimental data for the present system precludes a direct verification of this result by comparison to other experiments. However, the value is fully consistent with recent density functional theory calculations by Honkala and Laasonen, who derived an activation barrier of 54 kJ mol^{-1} on Pd (111).[45]

D. Influence of the surface temperature

In the next step, we investigate the surface temperature dependence of the angular distributions of CO_2, both under CO-rich and under O-rich conditions. The simulated angular distributions of CO_2 and the Θ_O profiles are displayed in Fig. 10. The model yields a weak dependence in the temperature range $440\leqslant T\leqslant 490$ K for both O-rich and CO-rich conditions. In the first case ($x_{CO}=0.34$) the angular distribution of CO_2 is almost symmetric at 490 K. There is a very slight decrease in the rate on the shaded particle side with decreasing surface temperature. Under CO-rich conditions ($x_{CO}=0.67$), the CO_2 distributions are asymmetric with an enhanced reaction rate on the particle side facing the O_2 beam. Under both sets of flux conditions, the asymmetry increases only weakly with decreasing temperature.

A comparison with the experimental data (Fig. 5) shows that the temperature dependence is well reproduced by the simulations. We can now obtain a deeper insight into the kinetic origin of the temperature dependence on the basis of the simulations.

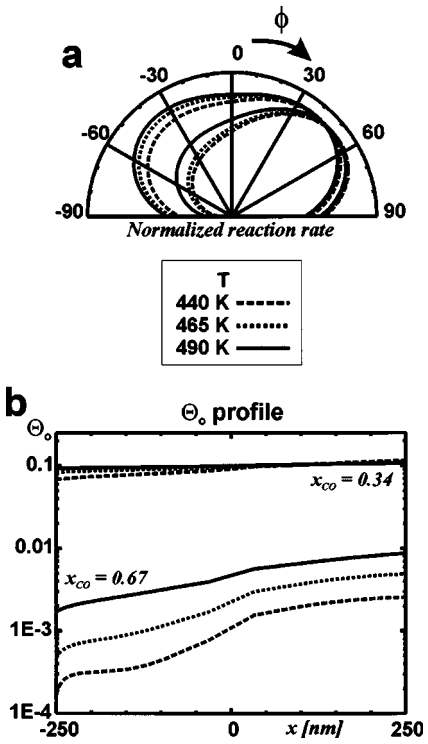

FIG. 10. Simulated data: Temperature dependence of (a) the angular distribution of CO_2 and (b) the Θ_O profiles [$T=440,465,495$ K, $E_{diff}=55$ kJ mol^{-1}, CO-rich ($x_{CO}=0.67$), and O-rich ($x_{CO}=0.34$) regimes].

As discussed before, the Θ_O profiles and consequently the CO_2 angular distributions are controlled by the oxygen diffusion length. The latter depends on two factors:[24] (i) the oxygen residence time, which depends on the O steady-state coverage and on the reaction rate, and (ii) the oxygen diffusion coefficient. Under O-rich conditions, Θ_O is high and the reaction rate is nearly independent of the surface temperature (CO adsorption is the rate determining step, Figs. 5 and 8). Therefore, the oxygen residence time is nearly independent of the surface temperature. In contrast, the diffusion coefficient D increases with increasing temperature (for $E_{diff}=55$ kJ mol^{-1}, $D_{490\ K}/D_{440\ K}=4.6$). However, the increase only has a moderate effect on the Θ_O profiles since the diffusion length is already larger than the particle size. As a result, the changes in the CO_2 angular distributions are weak.

The situation is more complicated in the CO-rich regime. Figures 8(a) and 10(b) show that both the reaction rate and Θ_O increase with increasing temperature. Oxygen dissociative adsorption is the rate determining step. The oxygen adsorption rate increases as Θ_{CO} decreases with increasing temperature. The changes in reaction rate and Θ_O compensate and lead to a weak temperature dependence of the residence time. The temperature dependence of the diffusion length is therefore mainly due to the diffusion coefficient. With the diffusion length (which is below the particle size) increasing with increasing temperature, the oxygen gradient decreases slightly and the asymmetry of the angular distribution becomes less pronounced. As a last point it should be noted that in the temperature interval considered the changes in Θ_O due to the temperature dependence of the diffusion length are considerably weaker than the changes which occur

upon switching between the reaction regimes (CO rich and O rich). Therefore, the CO_2 angular distributions are more sensitive to changes of x_{CO} than of the surface temperature.

E. Influence of backscattering effects from the support

The desired experimental information in the angular resolved experiments is carried primarily by those molecules which undergo no additional scattering processes with the surface. In practice, two additional channels have to be taken into account. First, the incident molecules can be diffusely backscattered from the support and subsequently collide with the metal particles. This leads to a diffuse flux of reactants towards the particles. Second, the reaction products desorbing from the side facets of the particles can collide with the support and can be backscattered into the vacuum. It is important to determine how these contributions affect the experimental results discussed in this work and to what extent they might complicate the extraction of information on local reaction rates.

In order to study the relevance of support backscattering contributions, we analyze these effects in detail in terms of the present kinetic model. We first investigate the effect of support backscattering in the incident reactant flux. In Figs. 7(b) and 7(c) the total CO and O_2 fluxes toward the particle surface are plotted for section of the particle along the x axis. The total flux contains two components, the direct beam contribution and the backscattering contribution. Whereas the direct flux is maximal at those parts of the particle directly facing the beams, the backscattering channel is most prominent at the particle edges. It is noteworthy that there are substantial differences in the backscattered fluxes of CO and O_2. For CO, the backscattered flux approaches a value of 50% of the maximum direct flux at the edge of the particle and vanishes on top. For O_2, a large fraction of the particle is shaded from a direct flux. The backscattered contribution from the support is also asymmetric due to the shadow on the support on the shaded side of the particle. As a result, the total O_2 flux on the shaded side is relatively low in spite of the support backscattering contribution. It is also noteworthy that support backscattering creates a zone at $x \approx -100$ nm where the flux has a local minimum.

In addition, the backscattering of the products is taken into account as described in Sec. IV A. Product backscattering simply adds a symmetric component to the angular distribution of CO_2. Thus, it only qualitatively affects the results [Fig. 7(e)].

It is now interesting to investigate the effects of both backscattering contributions on the total angular distribution. In Fig. 11, a comparison of the Θ_O profiles and CO_2 angular distributions is shown for a hypothetical case, in which support backscattering is completely neglected and for a case in which the effect is fully taken into account ($T=465$ K, $E_{diff}=55$ kJ mol^{-1}). Focusing on the Θ_O profiles first, the differences between the models are weak under O-rich conditions. This is the result of the rapid equilibration of Θ_O. Under CO-rich conditions however, the Θ_O gradient is significantly reduced by the support backscattering, because the backscattering of oxygen gives rise to a strong relative enhancement of the O_2 flux on the shaded side of the particle.

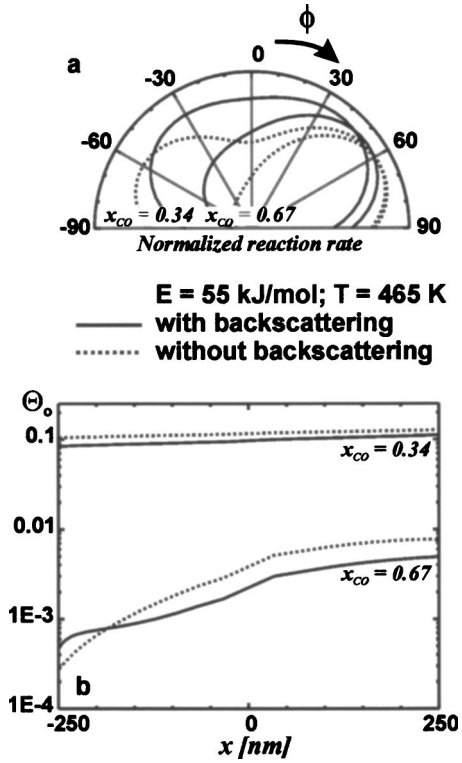

FIG. 11. Simulated data: (a) Effect of the backscattering on the angular distributions of desorbing CO_2 and (b) on the Θ_O profiles under O-rich ($x_{CO}=0.34$) and CO-rich ($x_{CO}=0.67$) conditions. The backscattering is either fully "switched on" or "off" for both the incident beams and the desorbing products.

In Fig. 11(a) the corresponding CO_2 angular distributions are displayed. Under both CO- and O-rich conditions, support backscattering results in a drastic modification of the angular distributions. Taking the previous discussion into account, it is apparent that under O-rich conditions the differences almost exclusively arise from product backscattering. The latter leads to a reduced width of the CO_2 distributions. For the CO-rich case, on the other hand, the differences result from both reactant and product backscattering. The effect is particularly strong on the O-shaded side, where backscattering tremendously enhances CO_2 production and thus effectively reduces the asymmetry of the distributions.

We now compare the calculated distributions and the experimental results from Fig. 5. It is found that the experimental data are well reproduced by the model including support backscattering. Conversely, the model neglecting the backscattering channel predicts artificially broad angular distributions and strongly overestimates the asymmetry of the angular distributions.

F. Influence of the local angular distribution of CO_2

A key point in the simulation of the angular distribution of CO_2 from a supported nanoparticle system is the angular distribution of CO_2 from a local surface element. From single crystal studies it is well known that such distributions may sensitively depend on many factors such as the local surface structure or the adsorbate coverages.[46] For the

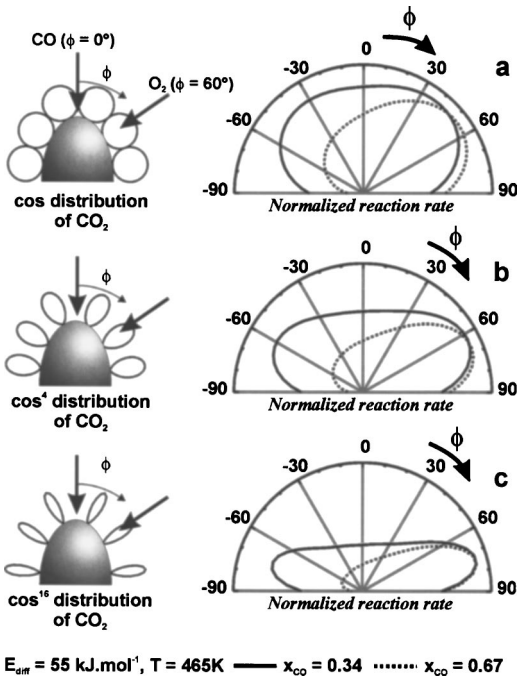

FIG. 12. Simulated data: Effect of the local angular distribution of CO_2 (modeled by a $\cos^n \phi$ distribution) on the total angular distribution of products desorbing from the particle (N.B.: the backscattered fluxes always follow a $\cos^1 \phi$ distribution) at $T=465$ K, $E_{\mathrm{diff}}=55$ kJ mol^{-1}. Values of $n=1$ (a), $n=4$ (b), and $n=16$ (c) are investigated under O-rich (full lines, $x_{\mathrm{CO}}=0.34$) and CO-rich (dotted lines, $x_{\mathrm{CO}}=0.67$) conditions. The figures on the right show the total angular distributions, assuming local $\cos \phi$, $\cos^4 \phi$, and $\cos^{16} \phi$ (top to bottom) CO_2 distributions.

present model catalyst, the prolonged heat treatment after preparation leads to reshaping of the particles, preferentially exposing low-index facets. Some experimental information is available for the angular distribution of CO_2 desorbing from such surfaces. On Pd(111), for example, it was found that in the limit of low coverage the CO_2 distribution is broad and well described by a cosine distribution.[26] In the limit of high Θ_O, however, much stronger peaking along the surface normal was observed.[30]

In the following, we investigate the role of the width of the local angular distribution on the total CO_2 distribution emitted by the supported catalyst. In the simulations, the local distribution of desorbing CO_2 is described by a function $\cos^n \phi$. Some representative results are given in Fig. 12, ranging from diffuse desorption ($n=1$) to highly directed desorption along the particle surface normal ($n=16$). It is found that the total CO_2 distribution becomes increasingly broad with increasing n. In spite of the strong dependence on the width of the local distribution, the qualitative picture remains unchanged, however: Under O-rich conditions the CO_2 distributions are symmetric, whereas they become strongly asymmetric in the CO-rich regime. Although the asymmetry shows the expected decrease with decreasing n, the effect remains clearly visible down to $n=1$.

Several conclusions follow from these results. First of all, it is apparent that a highly directed product desorption leads to a stronger asymmetry of the total CO_2 distribution. Therefore, a highly peaked local desorption is advantageous for the type of experiment discussed here. However, the angular dependent effects can be easily detected even in the case of very diffuse local distributions of desorbing products ($n=1$). Indeed, a comparison with the experimental distributions (Fig. 5) shows the best agreement for $n \approx 1$. Therefore we conclude that under the experimental conditions applied in this work, the local CO_2 distribution is well described by diffuse CO_2 desorption. With respect to the applicability of the method, this result demonstrates that angular dependent measurements of the type performed in this work should be feasible for many reaction systems, and do not require particularly narrow local angular distributions of desorbing products.

V. CONCLUSIONS

We have studied the angular distribution of desorbing CO_2 during CO oxidation on a supported palladium model catalyst using a combination of molecular beam methods and angular resolved mass spectrometry.

(1) The Pd model catalyst was prepared by electron beam lithography on a SiO_2 film on Si(100). Pd particles with ~500 nm diameter and an aspect ratio of nearly 1 were prepared on a perfect hexagonal lattice with a particle density of 5.1×10^7 cm^{-2}. A cleaning procedure was developed in order to remove contaminations from the particle surface.

(2) Molecular beam experiments were performed using a combination of CO and O_2 beams, establishing different local reactant fluxes on different parts of the particles. The two reaction regimes of the CO oxidation (CO rich and O rich) are characterized by specific angular CO_2 distributions. Under CO rich reaction conditions, the CO_2 distribution strongly depends on the local fluxes, whereas nearly symmetric distributions are observed under O-rich conditions. The angular distributions show a weak temperature dependence in the range between 440 and 490 K.

(3) The experimental results were quantitatively reproduced by a diffusion-reaction model, taking into account the geometry of the model catalyst and reactant and product backscattering effects from the support.

(a) The different angular distributions of CO_2 in the two reaction regimes were related to pronounced differences in the oxygen residence time. As a result, equilibration of Θ_O occurs under O-rich conditions only, and pronounced gradients in Θ_O are established under CO-rich conditions.

(b) By comparison of the experimental angular distributions with the simulations as function of the CO/O_2 ratio, we obtain an estimate for the activation energy for oxygen diffusion on the particle surface of (55 ± 10) kJ mol^{-1}.

(c) The model reproduces the weak temperature dependence of the angular distributions, which can be related to a partial compensation of the temperature dependences of the diffusion coefficient, the reaction rate and the steady-state coverages.

(d) By comparison with the experimental results it was shown that a quantitative description of the experiment requires trapping-desorption and direct scattering processes from the support to be taken into account, both for the incoming reactants and for the desorbing products. Support

backscattering is found to significantly broaden the angular distribution of desorbing products. In spite of this effect, strong angular dependences remain, which can be easily detected experimentally.

(e) Finally, the effect of the local angular distribution of CO_2 desorbing from a single particle facet on the total angular CO_2 distribution was investigated. The experimental data are consistent with a broad local distribution ($\cos^n \phi$ with $n \approx 1$). Other systems, with a more peaked product distribution, are expected to create even more pronounced angular dependent effects than observed in the present case.

The results suggest that angular resolved experiments of the type presented in this work can be quantitatively understood on the basis of a microkinetic diffusion-reaction model. The information on the distribution of reaction rates on the particle surface survives in spite of support scattering effects and diffuse local angular distributions of the desorbing products. As a result, information on kinetic parameters such as surface diffusion rates as well as on local reaction rates on supported nanoparticles can be extracted from a comparison of experiment and simulation.

ACKNOWLEDGMENTS

The authors acknowledge the support of the Deutsche Forschungsgemeinschaft and of the Competence Center for Catalysis at Chalmers, supported by the Swedish Energy Administration, Chalmers, and its member companies: AB Volvo, Johnson Matthey CSD, Saab Automobile Powertrain AB, Persorp AB, MTC AB, Eka Chemicals, and the Swedish Space Administration. M.L. thanks C. Beta (FHI Berlin) for helpful discussions. The authors thank G. Weinberg (FHI Berlin) for the SEM images of the lithographically prepared model catalyst.

[1] *Handbook of Heterogeneous Catalysis*, edited by G. Ertl, H. Knoezinger, and J. Weitkamp (VCH, Weinheim, 1997).
[2] J. M. Thomas and W. J. Thomas, *Principle and Practice of Heterogeneous Catalysis* (VCH, Weinheim, 1997).
[3] V. P. Zhdanov and B. Kasemo, J. Catal. **170**, 377 (1997).
[4] V. P. Zhdanov and B. Kasemo, Phys. Rev. B **55**, 4105 (1997).
[5] V. P. Zhadanov and B. Kasemo, Surf. Sci. **405**, 27 (1998).
[6] V. Johánek, M. Laurin, A. W. Grant, B. Kasemo, C. R. Henry, and J. Libuda, Science **304**, 5677 (2004).
[7] V. P. Zhdanov and B. Kasemo, Surf. Sci. **496**, 251 (2002).
[8] K. A. Fichthorn, E. Gulari, and R. M. Ziff, Phys. Rev. Lett. **63**, 1527 (1989).
[9] Y. Suchorski, J. Beben, E. W. James, J. Evans, and R. Imbihl, Phys. Rev. Lett. **82**, 1907 (1999).
[10] H.-J. Freund, M. Bäumer, J. Libuda, T. Risse, G. Rupprechter, and S. Shaikhutdinov, J. Catal. **216**, 223 (2003).
[11] H.-J. Freund, Surf. Sci. **500**, 271 (2002).
[12] H.-J. Freund, H. Kuhlenbeck, J. Libuda, G. Rupprechter, M. Bäumer, and H. Hamann, Top. Catal. **15**, 201 (2001).
[13] J. Libuda and H.-J. Freund, J. Phys. Chem. B **106**, 4901 (2002).
[14] C. R. Henry, Surf. Sci. Rep. **31**, 231 (1998).
[15] C. C. Chusuei, X. Lai, K. Luo, and D. W. Goodman, Top. Catal. **14**, 71 (2001).
[16] T. Hrncir, V. Matolin, and V. Nehasil, Surf. Sci. **482-485**, 260 (2001).
[17] K. Judai, S. Abbet, A. S. Worz, U. Heiz, and C. R. Henry, J. Am. Chem. Soc. **126**, 2732 (2004).
[18] M. Bowker, P. Stone, R. Bennett, and N. Perkins, Surf. Sci. **497**, 155 (2002).
[19] S. Johansson, L. Österlund, and B. Kasemo, J. Catal. **201**, 275 (2001).
[20] K. Wong, S. Johansson, and B. Kasemo, Faraday Discuss. **105**, 237 (1996).
[21] J. Grunes, J. F. Zhu, E. A. Anderson, and G. A. Somorjai, J. Phys. Chem. B **106**, 11463 (2002).
[22] A. S. Eppler, G. Rupprechter, L. Guczi, and G. A. Somorjai, J. Phys. Chem. B **101**, 9973 (1997).
[23] A. S. Eppler, J. Zhu, E. A. Anderson, and G. A. Somorjai, Top. Catal. **13**, 33 (2000).
[24] V. Johanek, M. Laurin, J. Hoffmann, S. Schauermann, A. W. Grant, B. Kasemo, J. Libuda, and H.-J. Freund, Surf. Sci. Lett. **561**, L218 (2004).
[25] J. Hoffmann, S. Schauermann, J. Hartmann, V. P. Zhdanov, B. Kasemo, J. Libuda, and H.-J. Freund, Chem. Phys. Lett. **354**, 403 (2002).
[26] T. Engel and G. Ertl, J. Chem. Phys. **69**, 1267 (1978).
[27] T. Engel and G. Ertl, in *The Chemical Physics of Solid Surfaces and Heterogeneous Catalysis*, edited by D. A. King and D. P. Woodruff (Elsevier, New York, 1982), Vol. 4, p. 73.
[28] E. G. Seebauer and C. E. Allen, Prog. Surf. Sci. **49**, 265 (1995).
[29] M. Snabl, O. Borusik, V. Chab, M. Ondrejcek, W. Stenzel, H. Conrad, and A. M. Bradshaw, Surf. Sci. Lett. **385**, L1016 (1997).
[30] T. Matsushima and H. Asada, J. Chem. Phys. **85**, 1658 (1986).
[31] X. Guo, A. Hoffman, and J. T. Yates, Jr., J. Chem. Phys. **90**, 5787 (1989).
[32] F. P. Leisenberger, G. Koller, M. Sock, S. Surnev, M. G. Ramsey, F. P. Netzer, B. Klötzer, and K. Hayek, Surf. Sci. **445**, 380 (2000).
[33] S. Johansson, K. Wong, V. P. Zhdanov, and B. Kasemo, J. Vac. Sci. Technol. A **17**, 297 (1999).
[34] J. Libuda, I. Meusel, J. Hartmann, and H.-J. Freund, Rev. Sci. Instrum. **71**, 4395 (2000).
[35] G. Comsa and R. David, Surf. Sci. Rep. **5**, 145 (1985).
[36] P. U. Andersson, M. B. Nagard, K. Bolton, M. Svanberg, and J. B. C. Pettersson, J. Phys. Chem. A **104**, 2681 (2000).
[37] J. Libuda, I. Meusel, J. Hoffmann, J. Hartmann, L. Piccolo, C. R. Henry, and H.-J. Freund, J. Chem. Phys. **114**, 4669 (2001).
[38] J. Hoffmann, I. Meusel, J. Hartmann, J. Libuda, and H.-J. Freund, J. Catal. **204**, 378 (2001).
[39] J. Hoffmann, S. Schauermann, V. Johánek, J. Hartmann, and J. Libuda, J. Catal. **213**, 176 (2003).
[40] V. P. Zhdanov, Surf. Sci. Rep. **45**, 233 (2002).
[41] V. P. Zhdanov and B. Kasemo, Surf. Sci. Rep. **39**, 25 (2000).
[42] S. Völkening and J. Wintterlin, J. Chem. Phys. **114**, 6382 (2001).
[43] V. Nehasil, T. Hrncir, S. Zafeiratos, S. Ladas, and V. Matolin, Surf. Sci. **454**, 289 (2000).
[44] V. Matolin and I. Stara, Surf. Sci. **398**, 117 (1998).
[45] K. Honkala and K. Laasonen, J. Chem. Phys. **115**, 2297 (2001).
[46] T. Matsushima, Surf. Sci. Rep. **52**, 1 (2003).